
CHAPTER 11

X-RAY OPTICS

James E. Harvey

*The Center for Research and Education in Optics and Lasers
(CREOL)*

*University of Central Florida
Orlando, Florida*

11.1 GLOSSARY

Acronyms

ACV	autocovariance function
AXAF	Advanced X-ray astrophysical facility
BBXRT	broadband x-ray telescope
EUV	extreme ultraviolet
FWHM	full-width at half-maximum
HPR	half-power-radius
HPR _G	geometrical half-power-radius
MTF	modulation transfer function
OTF	optical transfer function
PSD	power spectral density function
PSF	point spread function

Symbols

<i>I</i>	irradiance
<i>E</i>	electric field
<i>ε</i>	linear obscuration ratio
<i>f</i>	focal length
λ	wavelength

n	index of refraction
r_o	diffraction-limited (linear) image radius
θ_o	diffraction-limited (angular) image radius
D	aperture diameter
P	radiant power
A_n, A_t	effective collecting area
α, β, γ	direction cosines
σ_s, σ	root-mean-square surface roughness
σ_w	root-mean-square wavefront error
t	substrate thickness
l	autocovariance length
$P(x, y)$	complex pupil function
$H(x, y)$	optical transfer function
$H_s(x, y)$	surface transfer function
$C_s(x, y)$	surface autocovariance function
$S(\alpha, \beta)$	angle spread function

11.2 INTRODUCTION

The following fundamental difficulties have served as a deterrent to the development of x-ray imaging systems: adequate sources and detectors have not always been available; no suitable refractive material exists from which conventional x-ray lenses can be fabricated; mirrors have traditionally exhibited useful reflectances only for grazing incident angles; grazing incidence optical designs are cumbersome and difficult to fabricate and align; scattering effects from imperfectly polished surfaces severely degrade image quality for these very short wavelengths; and finally, the absorption of x-rays by the atmosphere limits practical applications to evacuated propagation paths in the laboratory or to space applications.

New technologies such as synchrotron sources, free electron lasers, and laser-generated plasmas are being developed.^{1–5} Improved optical fabrication techniques and the rapidly emerging technology of enhanced reflectance x-ray multilayers are therefore resulting in a resurgence of activity in the field of x-ray and extreme ultraviolet (EUV) imaging systems.^{6–9} These significant advances are stimulating renewed efforts in the areas of x-ray/EUV astronomy, soft x-ray microscopy, and x-ray microlithography.^{10,11}

In this chapter we will first review the historical background of x-ray optics. The reader will then be warned about several potential pitfalls in the design of x-ray/EUV imaging systems; in particular, it will be emphasized that scattering effects from optical fabrication errors almost always dominate residual optical design errors at these very short wavelengths. The optical performance of x-ray/EUV optical systems will be discussed from a systems engineering viewpoint and a technique of error-budgeting will be discussed. Diffraction effects will be shown to be a significant source of image degradation for certain grazing incidence x-ray optics applications. Scattering effects will be discussed in detail and characterized by an effective surface transfer function. And x-ray multilayers will be shown to act as a surface power spectral density (PSD) filter function. Our

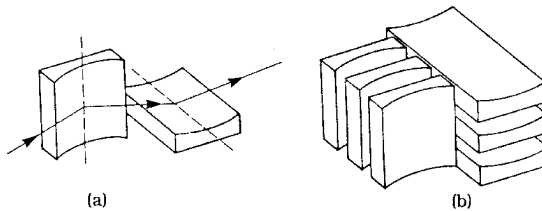


FIGURE 1 (a) The Kirkpatrick-Baez telescope consists of two orthogonal grazing incidence parabolic sheet mirrors; (b) a multiplate stack of several mirrors can be used to substantially increase the collecting area.

understanding of the combined effect of diffraction, geometrical aberrations, and scattering will then be demonstrated by making accurate image quality predictions for a variety of applications of interest. Finally, a brief summary and conclusion will be presented.

11.3 HISTORICAL BACKGROUND

Grazing Incidence X-ray Imaging Systems

The first two-dimensional image produced by deflecting rays in a controlled manner was obtained by Kirkpatrick and Baez in 1948 with two grazing incidence mirrors as illustrated in Fig. 1(a).¹² The extremely small collecting area of such an imaging system can be alleviated by constructing the multiplate Kirkpatrick-Baez mirror of Fig. 1(b).

In 1952 Wolter published a paper in which he discussed several rotationally symmetric grazing incidence x-ray telescope systems.¹³ The Wolter Type I telescope consists of a coaxial paraboloid (primary mirror) and hyperboloid (secondary mirror) as illustrated in Fig. 2(a). The focus of the paraboloid is coincident with the rear focus of the hyperboloid.

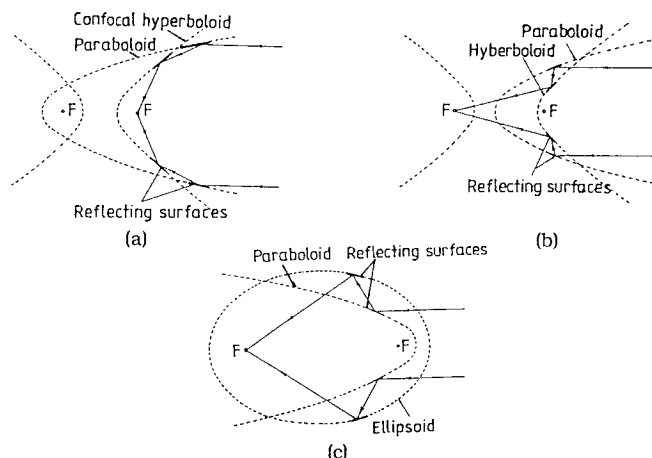


FIGURE 2 (a) Wolter Type I telescope; (b) Wolter Type II telescope; (c) Wolter Type III telescope.

and the reflection occurs on the inside of both mirrors. The Wolter Type II telescope also consists of a coaxial paraboloid and hyperboloid. However, the focus of the paraboloid is coincident with the front focus of the hyperboloid and the reflection occurs on the inside of the paraboloid and the outside of the hyperboloid. This system is the grazing incidence analog to the classical Cassegrain telescope. The Wolter Type III telescope consists of a paraboloid and an ellipse. The focus of the paraboloid is coincident with the front focus of the ellipse, and the reflection occurs on the outside of the paraboloid and on the inside of the ellipse. The Wolter Type I telescope typically has a grazing angle of less than a degree and is used for hard x-rays (greater than 1 keV). The Wolter Type II telescope typically has a grazing angle of approximately 10 degrees and is used for soft x-rays and the extreme ultraviolet (EUV).

These grazing incidence optical configurations are free of spherical aberration; however, they exhibit severe field curvature, coma, and astigmatism. They are also quite cumbersome to fabricate and require a huge surface area to achieve a very small collecting area. Furthermore, at these extremely short wavelengths, very smooth surfaces are required to prevent scattering effects from severely grading the resulting image quality. Aschenbach has presented a nice review of these scattering effects in x-ray telescopes.¹⁴

Primarily due to much improved optical surface metrology capabilities, the conventional optical fabrication techniques of grinding and polishing glass substrates are resulting in major advances in the resolution of grazing incidence x-ray telescopes.^{15,16} The European ROSAT (Röntgensatellit) telescope¹⁷ consisting of four nested Wolter Type I grazing incidence telescopes provides substantial improvement in both effective collecting area and resolution over the Einstein Observatory which was launched in 1978,^{18,19} and the technology mirror assembly (TMA)²⁰ for NASA's advanced X-ray Astrophysical Facility (AXAF)²¹ has demonstrated that the technology exists to produce larger Wolter Type I grazing incidence x-ray telescopes with subarcsecond resolution. This progress in grazing incidence x-ray optics performance is illustrated graphically in Fig. 3.²² A Wolter Type II telescope capable of achieving a half-power-radius of 0.5 arcsec at a wavelength of 1000 Å is currently being studied for use in NASA's Far Ultraviolet Spectroscopic Explorer (FUSE) program.²³

The very smooth surfaces required of high-resolution x-ray optics have been achieved by tedious and time-consuming optical polishing efforts of skilled opticians. AXAF and

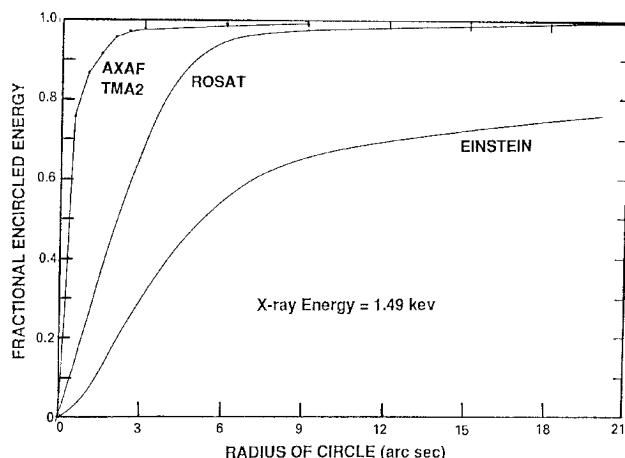


FIGURE 3 Fractional encircled energy plots at 1.49 keV for the Einstein Observatory, the European ROSAT telescope, and the AXAF technology mirror assembly (TMA2) are compared.

ROSAT are thus very expensive to produce. Less labor-intensive (and therefore less expensive) optical fabrication techniques such as plasma-assisted chemical etching (PACE) are therefore being developed.²⁴

When such high resolution is not required, other optical materials and fabrication techniques may be applicable. The extreme ultraviolet explorer (EUV) is a NASA-funded astronomy mission intended to perform an all-sky survey in the 70- to 760-Å spectral region. The deep survey and spectroscopic portion of the mission utilizes a Wolter Type II grazing incidence telescope built at the Space Sciences Laboratory at the University of California, Berkeley. Its mirrors were fabricated from aluminum substrates by forging, rough machining, diamond turning to the desired figure, nickel plating, polishing, and coating with gold. An image half-power-width of approximately 15 arcsec was achieved.²⁵

Smooth x-ray mirror surfaces have been achieved without any labor-intensive polishing by merely dipping diamond-turned metal substrates in lacquer, then depositing tungsten or gold coatings to yield the desired high reflectance.^{26,27}

The apparent smoothness of the lacquer-coated surfaces and a desire for light weight and a high throughput or filling factor led Petre and Serlemitsos to develop the concept of tightly nested conical foil x-ray telescopes.²⁸ Conical x-ray imaging mirrors represent the long focal length limit of Wolter Type I grazing incidence mirrors; i.e., the departure of the paraboloid and hyperboloid from simple cones diminishes with increasing focal length. The technology to fabricate and assemble many concentric, nested conical foil x-ray telescopes for high-throughput, moderate resolution, spectroscopic applications has been described in detail. This technique consists of dipping metal foil substrates in lacquer to obtain the optical surface, coating them with gold, then precisely positioning them in a fixture to comprise a tightly packed concentric array of individual telescopes to achieve a relatively high aperture filling factor. The NASA/GSFC broadband x-ray telescope (BBXRT), consisting of 101 concentric conical foil mirror pairs, has recently provided the first flight data from an instrument of this type.²⁹ Scientists at the Danish Space Research Institute (DSRI) are currently fabricating and testing similar mirrors for the XSPEC telescope being developed for the Soviet Spectrum-X-Gamma mission.³⁰ This telescope will have 154 concentric shells with grazing angles varying from 9 to 33 arcmin. The Japanese are planning an x-ray telescope mission called SXO in which 89 concentric foil shells will be utilized.³¹

Still other novel optical fabrication concepts for grazing incidence x-ray optical surfaces include a variety of replication techniques.³² The Italian x-ray astronomy satellite (SAX) will consist of 30 nested coaxial mirrors electroformed over conical mandrels to a thickness ranging from 0.2 to 0.4 min.³³ Finally, the European Space Agency (ESA) will provide a dramatic increase in collecting area with its high throughput x-ray spectroscopy XMM mission featuring several modules of 58 tightly nested confocal Wolter Type I telescopes fabricated with a metal/epoxy replication technique.³⁴

Normal Incidence X-ray Multilayers

The possibility of obtaining enhanced reflectance of soft x-rays by multilayer structures was recognized soon after the discovery of x-ray diffraction by crystals. The first successful x-ray multilayers were obtained by Du Mond and Youtz in 1935 by vapor deposition of gold and copper with periods of approximately 100 Å.^{35–36} These multilayers turned out to be metallurgically unstable, interdiffusing over a period of a few weeks. In the 1960s, Dinklage and Frerichs fabricated lead/magnesium, gold/magnesium, and iron/magnesium multilayers with periods of 30 to 50 Å which were stable for approximately a year.^{37–38}

These multilayer structures were intended for use as dispersion elements in soft x-ray spectroscopy. In 1972, Spiller proposed that quarter-wave stacks of scattering/absorbing materials deposited by thermal-source vapor deposition techniques could be used to develop normal-incidence imaging systems in the EUV.³⁹⁻⁴¹ In 1976, Barbee and Keith reported upon sputter deposition techniques for producing multilayer structures on the atomic scale at a Workshop on X-ray instrumentation for Synchrotron Radiation.⁴²

The field of normal-incidence x-ray multilayer optics has advanced at a very rapid pace during the last 15 years. There are now over 40 groups worldwide actively working on x-ray multilayers for applications in soft x-ray astronomy, microscopy, microlithography, and synchrotron source experiments.⁴³⁻⁴⁷ Perhaps the most dramatic demonstration of the capabilities of normal-incidence x-ray multilayers to date was provided by the solar corona images obtained with the Stanford/MSFC Multispectral Solar Telescope Array. This 63.5-mm-diameter spherical Cassegrain telescope produced spectroheliograms with approximately 1 arcsec resolution at a wavelength of 171 Å.⁴⁸

These developments permit the return from the Wolter Type grazing incidence x-ray telescope designs to “classical” design forms such as the newtonian (prime focus paraboloid) and cassegrainian telescopes.⁴⁹

11.4 OPTICAL PERFORMANCE OF X-RAY/EUV IMAGING SYSTEMS

There has long been a desire to come up with a simple single-number merit function for characterizing the optical performance of imaging systems. However, the proper criterion for evaluating optical performance depends upon a number of different factors: the nature of the source or object to be imaged, the nature of the detector or sensor to be used, and the goal of the particular application.

Image Quality Criteria

The Strehl ratio is a common image quality criterion for near diffraction-limited imaging systems, but is completely inappropriate for some applications. The full width at half maximum (FWHM) of the point spread function (PSF) has been the astronomers’ classical definition of *resolution* and is quite appropriate when observing bright point sources; however, the optical transfer function (OTF) is a much more appropriate image quality criterion if the application involves studying fine detail in extended images (such as x-ray solar physics experiments and many soft x-ray microscopy applications). Soft x-ray projection lithography deals with imaging very specific object features which are best evaluated in terms of the square wave response (modulation in the image of a three-bar target) at a particular wavelength and spatial frequency. Fractional encircled energy of the PSF has become a very common image quality requirement imposed upon optical system manufacturers in recent years. Fractional encircled energy is a particularly relevant image quality criterion for some x-ray astronomy programs and for many x-ray synchrotron beamline applications where the imaging system is used to collect radiation and concentrate it on the slit of a spectrographic instrument.

Since the PSF is the squared modulus of the Fourier transform of the complex pupil function, the autocorrelation theorem from Fourier transform theory allows us to define

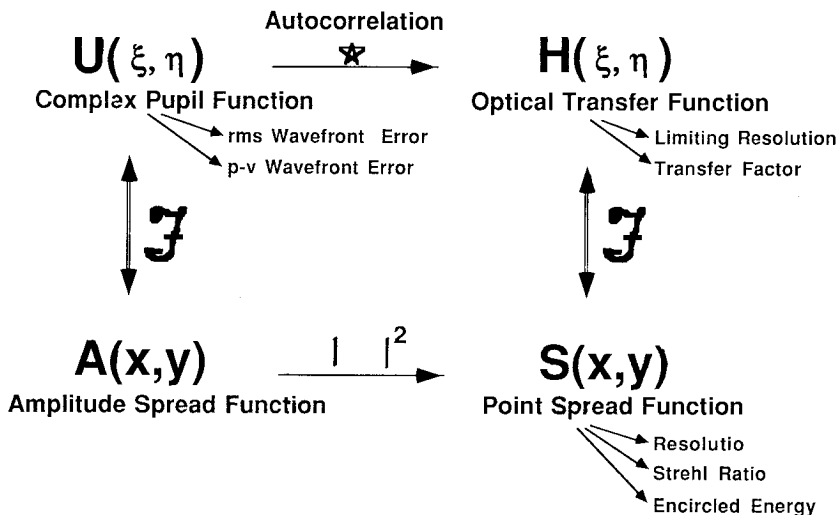


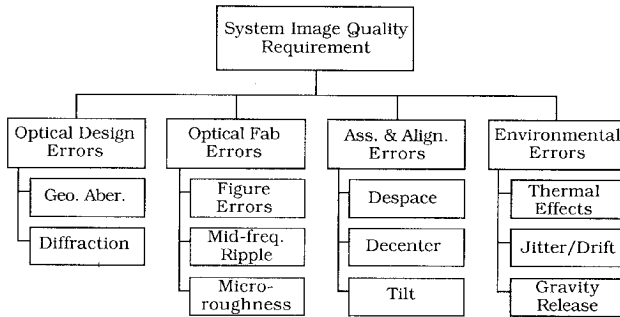
FIGURE 4 Some frequently used image quality criteria are properties of the complex pupil function. Others are obtained from the PSF or the OTF. This figure shows the relationship between these different image quality criteria.

the OTF as the normalized autocorrelation of the complex pupil function and to draw the relationship illustrated in Fig. 4.⁵⁰

The complex pupil function describes the wavefront aberrations that degrade image quality and, furthermore, these wavefront aberrations are rendered observable and measurable by interferometric techniques. Single-number merit functions derivable from interferometric data include the rms wavefront error and the peak-to-valley wavefront error. The amplitude spread function is not an observable quantity with ordinary sensors. The PSF is the irradiance distribution making up the image of an ideal point source. Frequently used single-number merit functions obtained from the PSF are the resolution, Strehl ratio, and the fractional encircled energy. The OTF contains all of the information about the spatial frequency content of the image. Limiting resolution and the transfer factor at a specific spatial frequency are single-number merit functions derivable from the OTF.

Potential Pitfalls in the Design and Analysis of X-ray/EUV Optics

There are many error sources in addition to residual design errors (geometric aberrations) that can limit the performance of high-resolution, short-wavelength imaging systems. Potential pitfalls in the design and analysis of x-ray/EUV imaging systems include: (1) assuming negligible diffraction effects at x-ray wavelengths; (2) overlooking the effects of ghost images in grazing incidence x-ray/EUV systems; (3) assuming that residual design errors dominate optical fabrication errors at these very short wavelengths; and (4) assuming that high reflectance implies negligible scattering in x-ray multilayers. Each of these potential pitfalls in the design and analysis of high-resolution x-ray/EUV imaging systems will be discussed and illustrated by examples in current programs of major interest.

**FIGURE 5** Error budget tree form.

Systems Engineering and the Error Budget Tree

The best way to avoid the above pitfalls is to take a systems engineering approach in the design and analysis of x-ray/EUV imaging systems and develop an error budget tree which includes all possible error sources. Figure 5 illustrates one form of an error budget tree that shows these error sources grouped into four main categories: optical design errors (including diffraction effects), optical fabrication errors (including scattering effects from surface irregularities over the entire range of relevant spatial frequencies), assembly and alignment errors, and environmental errors.

The top-level requirement should be expressed in terms of an appropriate image quality criterion for the particular application. Allocations for the individual error sources should then be determined by detailed analysis so that an equitable distribution of difficulty is achieved.

In general, as the wavelength becomes shorter and shorter, diffraction effects will diminish and scattering effects will be enhanced, while the geometrical aberrations are independent of wavelength. Since even the best optical surfaces are not always “smooth” relative to these very short wavelengths, optical fabrication errors will frequently dominate geometrical design errors in the degradation of image quality. Traditional optical design and analysis techniques (geometrical ray tracing) are therefore frequently inadequate for predicting the performance of high-resolution imaging systems at these very short wavelengths.

An error budget tree of this form is useful not only for the initial allocation of allowable errors from which specified tolerances can be derived, but also as a living tool for tracking achievements during the fabrication and alignment process. Occasional reallocation of the remaining error sources can then be made to assure that the system performance goals are met while minimizing the cost and schedule to complete the project.

11.5 DIFFRACTION EFFECTS OF GRAZING INCIDENCE X-RAY OPTICS

Diffraction effects of x-ray optical systems are often (justifiably) ignored due to the small wavelength of the x-ray radiation. However, the extremely large obscuration ratio inherent to grazing incidence optical systems produces profound degradation of the diffraction image over that produced by a moderately obscured aperture of the same diameter.⁵¹

Diffraction Behavior of Highly Obscured Annular Apertures

The diffraction-limited imaging performance of annular apertures has been discussed in detail by Tschunko.⁵² The irradiance distribution of an aberration-free image formed by an annular aperture with a linear obscuration ratio of ε is given by the expression

$$I(x) = \frac{1}{(1 - \varepsilon^2)^2} \left[\frac{2J_1(x)}{x} - \varepsilon^2 \frac{2J_1(\varepsilon x)}{\varepsilon x} \right]^2 \quad (1)$$

For large obscuration ratios, the cross terms in the above squared modulus represent a dominant interference effect that produces an irradiance distribution made up of ring groups as illustrated in Fig. 6.

Tschunko shows that, for $\varepsilon > 0.8$, the number of rings in each ring group is given by

$$n = \frac{2}{(1 - \varepsilon)} \quad (2)$$

Furthermore, 90 percent of the energy is contained within the first ring group and 95 percent within the second ring group, independent of the obscuration ratio. This is compared to 84 percent of the energy in the central lobe of the Airy pattern produced by

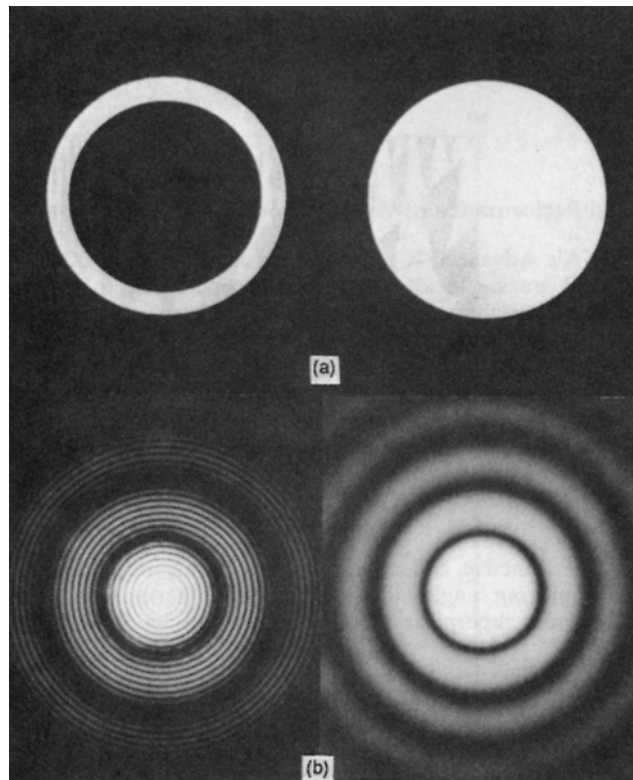


FIGURE 6 (a) A highly obscured annular aperture and an unobstructed circular aperture; (b) their respective Fraunhofer diffraction patterns.

an unobscured circular aperture. The central ring group clearly replaces the Airy disc as the meaningful image size. The central lobe itself contains a very small fraction of the energy and in no way represents a meaningful image size or resolution. This is particularly true for the incoherent superposition of images from a nested array of annular subapertures where the spacing of the ring structure varies for each element of the array. Also, small amounts of jitter or optical fabrication error will tend to smear the ring structure without significantly affecting the size of the central ring group or the fraction of energy contained within it.

Tschunko also points out that the minima between the ring groups are regularly spaced and the radii are equal to the number of rings multiplied by π , or

$$\text{Diffraction-limited image radius} = x_o = \pi n = \frac{2\pi}{(1 - \varepsilon)} \quad (3)$$

However, the actual radius of the diffraction image is obtained by setting

$$x = \frac{\pi r}{\lambda f/D} \quad (4)$$

hence

$$r_o = \frac{2\lambda f/D}{1 - \varepsilon} \quad (5)$$

or the angular radius containing 90 percent of the energy is

$$\theta_o = \frac{2\lambda/D}{1 - \varepsilon} \quad (6)$$

Diffraction-limited Performance of Wolter Type I X-ray Telescopes

NASA's Advanced X-ray Astrophysical Facility (AXAF) consists of six concentric Wolter Type I grazing incidence x-ray telescopes. Due to the severe field curvature and off-axis geometrical aberrations characteristic of grazing incidence telescopes,^{53,54} several alternative AXAF optical designs that were shorter and more compact and would therefore exhibit more desirable geometric image characteristics were proposed.^{55,56} However, to maintain a viable effective collecting area, many more nested shells had to be incorporated, as shown in Fig. 7.

Since the obscuration ratio of each Wolter Type I shell in the AXAF baseline design is 0.98, the diffraction-limited angular radius of the resulting image is given by

$$\theta_n = 100 \lambda / D_n \quad (7)$$

The effective collecting area of grazing incidence telescopes varies substantially with both grazing angle and x-ray energy; hence, the composite image made up of the incoherent superposition of the images produced by the individual shells is given by

$$\theta_o = \frac{1}{A_{t,n=1}} \sum_{n=1}^N A_n \theta_n \quad (8)$$

where A_t is the total effective collecting area for a given x-ray energy.⁵⁷

At least three different alternative optical designs with 18, 26, and 36 nested Wolter Type I shells were proposed for AXAF. The obscuration ratio, and therefore the diffraction-limited optical performance of these alternative optical designs, are substantially different. Figure 8 illustrates the predicted rms image radius as a function of x-ray

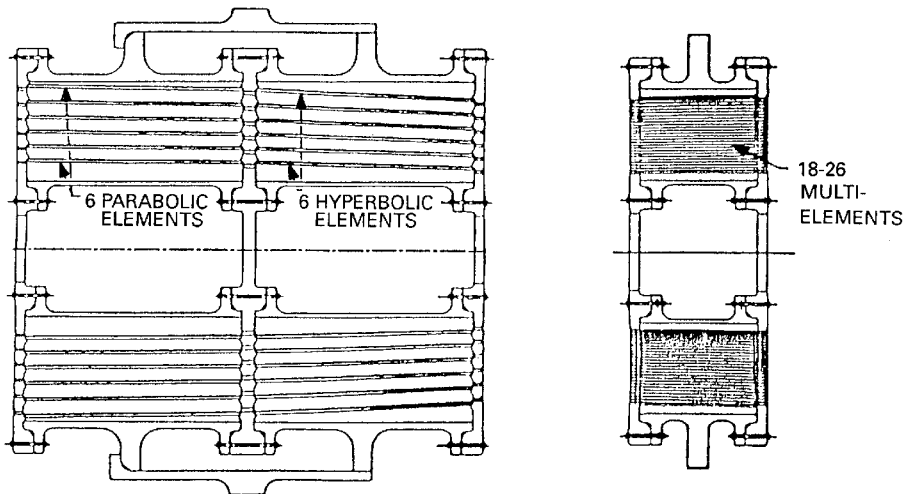


FIGURE 7 NASA baseline AXAF optical design and an alternative design with 18 to 26 concentric shells.

energy for each of these alternative designs plus the baseline design. The rms image radius was calculated from the radius θ_o of the first ring group (which contains 90 percent of the energy) by assuming a Gaussian image distribution with an encircled energy of 90 percent at $\theta = \theta_o$. This is a reasonable assumption since the final image distribution can be portrayed as the convolution of the image distribution due to a variety of error sources, and the central limit theorem of Fourier transform theory states that the convolution of N arbitrary functions approaches a Gaussian function as N approaches infinity.

The entire AXAF telescope error budget allocation (which must include optical

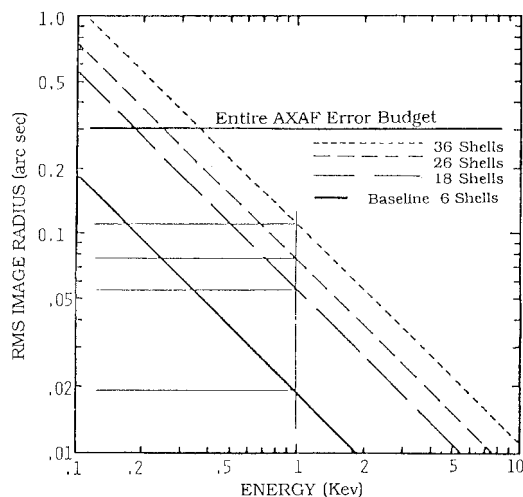


FIGURE 8 Diffraction-limited image quality of various AXAF optical designs.

fabrication, assembly, alignment, environmental, and long-term material stability errors as well as optical design errors) is also indicated in Fig. 8. The diffraction-limited image size for the NASA baseline design is negligible for x-ray energies greater than 1 keV; below 1 keV, diffraction rapidly becomes a dominant error source; and for the x-ray energy of 0.1 keV, it consumes a very significant fraction of the entire error budget. Note also that diffraction alone will prevent all three of the alternative designs from satisfying the top-level AXAF image quality requirement at the low-energy end of the AXAF spectral range.

Diffraction Effects of Nested Conical Foil Imaging Mirrors

Conical x-ray imaging mirrors represent the long focal length limit of Wolter Type I grazing incidence mirrors; i.e., the departure of the paraboloid and hyperboloid from simple cones diminishes with increasing focal length. A conical design and fabrication technique for the many nested thin-walled cones necessary to achieve a relatively high aperture filling factor has been described in Ref. 28.

This conical approximation to the ideal surface figure of the conventional Wolter Type I design results in a field-independent image degradation due to spherical aberration. By going to a short, compact design, the field curvature, coma, and astigmatism can be reduced to the point that they are dominated by the spherical aberration, thus resulting in a constant spatial resolution across the field of view. In Ref. 28, Petre and Serlemitsos have determined the geometrical optical performance of several conical x-ray telescope designs by utilizing a Monte Carlo ray-tracing procedure. In their conclusion they state that it is possible to design a conical foil telescope with arbitrarily high intrinsic spatial resolution by merely reducing the length of the mirror elements and increasing their number to maintain an acceptable effective collecting area. This, of course, increases the obscuration ratio and the corresponding image degradation due to diffraction.

Table 1 lists the design parameters taken from Ref. 28 for the NASA/GSFC BBXRT prototype mirror and a conical mirror assembly with the AXAF diameter and focal length.

The five parameters f , W , R_o , R_i , and t (defined in Table 1) completely define the conical mirror design, and the number of concentric shells N_t is then determined by the geometry; alternatively, given N_t , either R_o or R_i becomes constrained. Also tabulated is the predicted spatial resolution expressed as the angle within which half of the geometrically reflected rays fall. Petre and Serlemitsos also state that the axial spatial resolution may be expressed as

$$HPR_G = KWR_o^2/f^2 \quad (9)$$

where K depends weakly upon t and R_i .

From the above design parameters, one can calculate the minimum obscuration ratio of the individual nested shells making up these two x-ray telescope designs. The obscuration ratio for the BBXRT prototype is 0.9934 and that for the AXAF application is 0.9988.

TABLE 1 Nested Conical Foil Design Parameters²⁸

Design parameter	BBXRT prototype	AXAF application
f (focal length)	380 cm	1000 cm
W (length of each mirror)	10.0 cm	5.0 cm
R_o (radius of outer shell)	20 cm	60 cm
R_i (radius of inner shell)	8.9 cm	30 cm
t (substrate thickness)	0.17 mm	0.17 mm
N_t (number of shells)	101	900
HPR_G (half-power-radius)	12 arcsec	3 arcsec

These are extremely high obscuration ratios and may result in significant diffraction effects for some x-ray energies of interest.

Harvey has shown that diffraction effects are negligible compared to the geometrical HPR for the BBXRT design.⁵¹ However, suppose that we want to achieve a higher resolution. Petre and Serlemitsos state that virtually any intrinsic spatial resolution is possible by merely reducing W and increasing N_t to maintain an acceptable effective collecting area. This, of course, increases the obscuration ratio and the corresponding image degradation due to diffraction. Since the intrinsic image size is obtained by convolving these two independent contributions for each shell and calculating the effective area weighted average for all of the shells, a crossover point, beyond which diffraction is the dominant mechanism limiting the intrinsic resolution of the nested conical imaging telescope, is reached. We refer to *intrinsic resolution* as the image size produced by design parameters alone, assuming no image degradation due to fabrication errors, assembly and alignment errors, environmental errors, etc. Figure 9 illustrates the angular resolution (expressed as a half-power-radius) obtained by root-sum-squaring the geometrical half-power radius and the diffraction-limited half-power radius for several different conical mirror element lengths (W) as a function of x-ray energy. Clearly it is impossible to produce a telescope with these design parameters resulting in a resolution better than approximately 2.5 arcsec for 1 keV x-rays.

There is widespread international activity in the design and fabrication of grazing incidence x-ray telescopes, with particular interest in tightly nested conical foil designs. Furthermore, diffraction effects do not appear to be widely recognized as a potential limitation to spatial resolution in x-ray imaging systems. We have shown here that diffraction alone can prevent grazing incidence x-ray telescopes from meeting the desired optical performance requirements. However, just as diffraction can dominate geometrical aberrations in these grazing incidence imaging systems, we will soon see that scattering effects and alignment errors will almost always dominate both diffraction and geometrical aberrations.

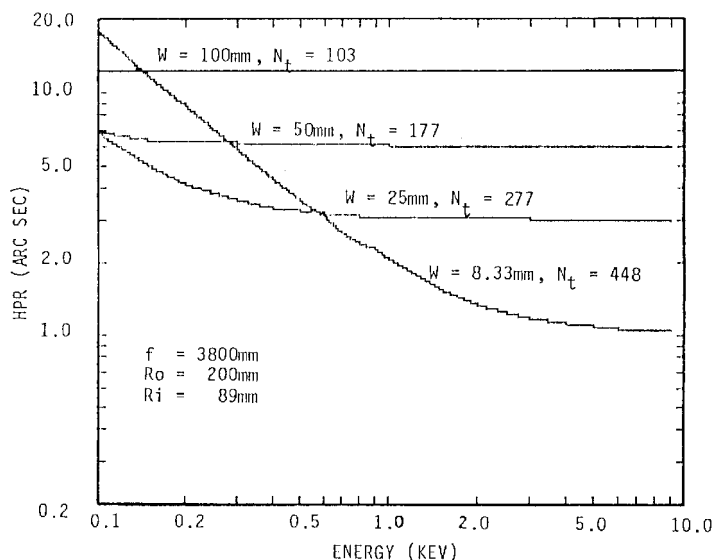


FIGURE 9 Parametric curves illustrating the tradeoff between geometrical effects and diffraction effects in the image size as the BBXRT mirror elements are shortened in an attempt to improve angular resolution.

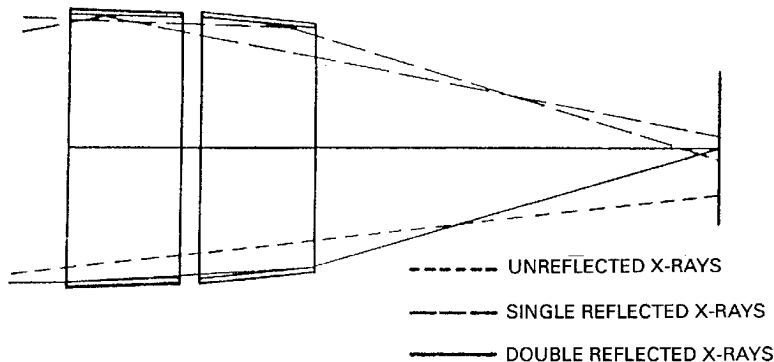


FIGURE 10 Ghost images in Wolter Type I telescopes are caused by x-rays which originate from out-of-field sources and reach the focal plane without being reflected from both mirrors.

11.6 GHOST IMAGES IN GRAZING INCIDENCE X-RAY TELESCOPES

Images are formed in Wolter Type I grazing incidence telescopes by x-rays which are reflected from both the primary and the secondary mirrors before reaching the focal plane. Ghost images result from rays which originate from out-of-field sources and reach the focal plane without being reflected from both mirrors as illustrated in Fig. 10.

When ghost images strike the focal plane near the optical axis, they can seriously degrade the quality of the desired image. Because of the extreme grazing angles of the Wolter Type I telescopes, ghost images are difficult to control by conventional aperture plates and baffles.

Aperture plates are usually required in a Wolter Type I system for the structural purpose of mounting and supporting the cylindrical mirrors. There are frequently conflicting demands placed upon the design of these aperture plates by requirements on field of view, vignetting, and ghost image control. Moran and Harvey have discussed the five different positions of aperture plates illustrated in Fig. 11 for use in the control of ghost images in Wolter Type I telescopes.⁵⁸

The spot diagrams in Fig. 12 were generated as aperture plates, sequentially added to a Wolter Type I system. The system focal length was 1000 cm and the mirrors were 80 cm

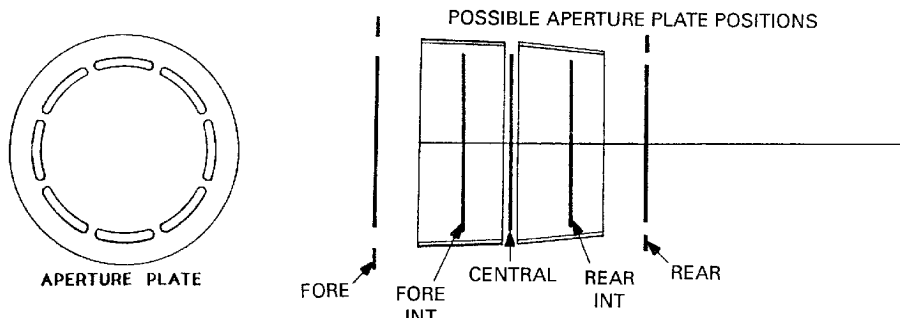


FIGURE 11 There are five different locations for aperture plates in the control of ghost images in Wolter Type I telescopes.

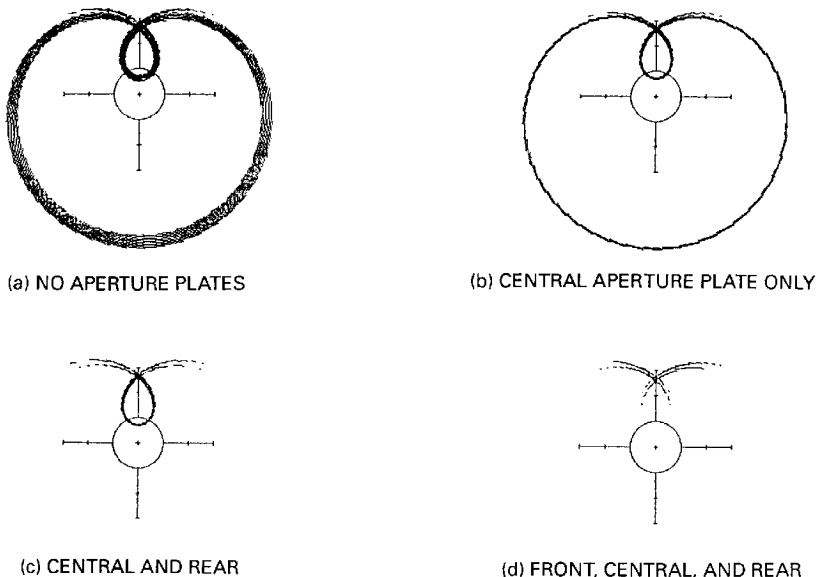


FIGURE 12 Ghost image characteristics as aperture plates are sequentially added to a Wolter Type I telescope.

long with a nominal diameter of 60 cm. This results in a grazing angle of approximately 0.43 degrees. These spot diagrams qualitatively demonstrate the relationship between ghost image characteristics and aperture plate position. The distribution of singly reflected ghost images from a point source at a field angle of 40 min of arc when no aperture plates are present is shown in Fig. 12(a). The circle centered on the optical axis in the focal plane is 15 min of arc in radius and represents the field within which we would like to exclude all ghost images.

The addition of a central aperture plate which does not introduce any vignetting thins out the ghost image distribution by blocking many of the singly-reflected rays, as shown in Fig. 12b. If we now add an aperture plate at the rear of the hyperboloid that satisfies a given vignetting requirement, we obtain the ghost image distribution shown in Fig. 12c. Notice that the ghost images furthest from the optical axis have been blocked. Finally, if we add a front aperture plate in front of the paraboloid which satisfies the same vignetting requirement, the ghost image distribution shown in Fig. 12d is produced. This fore aperture plate has eliminated the ghost images closest to the optical axis.

The position of the fore aperture plate (which blocks the ghost images closest to the optical axis in the focal plane) is a critical parameter in ghost image control. To obtain the ghost image pattern shown in Fig. 12d, the fore aperture plate was placed 100 cm in front of the primary mirror. This long distance would result in rather cumbersome and unwieldy aperture plate support structure. Figure 13 illustrates the ghost image behavior as a function of this fore aperture plate position. Note that 50 cm is the shortest distance in front of the primary mirror that the front aperture plate can be placed in order to eliminate all ghost images from a 20-arcmin semifield angle.

It is impractical to place aperture plates in front of each concentric shell of the tightly nested, high-throughput conical foil x-ray telescopes. A full analysis of the geometrical ghost imaging characteristics has thus been performed for the Soviet XSPEC and it was determined that it would be impossible to completely eliminate ghost images within a 10-arcmin radius of the optical axis in the focal plane.⁵⁹

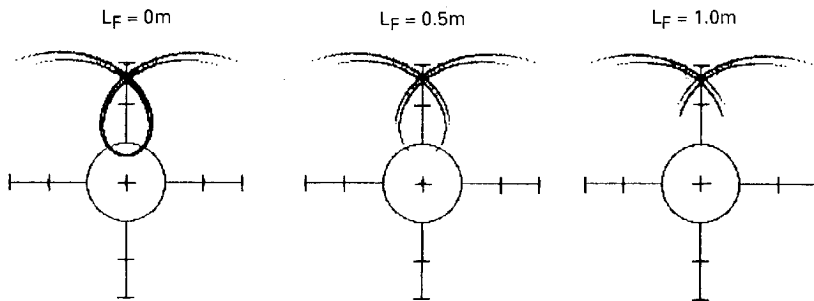


FIGURE 13 Illustration of ghost image distribution for various positions of the fore aperture plate.

Ghost image behavior is also a major concern for Wolter Type II telescopes. They typically have grazing angles of approximately 10 degrees and also require unconventional techniques for stray radiation control. Mangus has developed a strategy and calculations for the design of baffles for Wolter Type II telescopes.⁶⁰

11.7 SCATTERING EFFECTS FROM OPTICAL FABRICATION ERRORS

When light is reflected from an imperfect optical surface, the reflected radiation consists of a specularly reflected component and a diffusely reflected component as illustrated in Fig. 14. The light scattered from optical surface irregularities degrades optical performance in several different ways: (1) it reduces optical throughput since some of the scattered radiation will not even reach the focal plane, (2) the wide-angle scatter will produce a veiling glare which reduces image contrast or signal-to-noise ratio, and (3) the small-angle scatter will decrease resolution by producing an image blur.

It is customary to present angular scattering data as scattered intensity (flux per unit solid angle) versus scattering angle. Figure 15a illustrates several scattered light profiles from a polished and aluminized fused quartz sample. The results confirm the well-known fact that the scattered light distribution changes shape drastically with angle of incidence, becoming quite skewed and asymmetrical at large angles of incidence. However, if we take these scattered intensity curves and divide by the cosine of the scattering angle, then replot as a function of $\beta - \beta_o$, where $\beta = \sin \theta$ and $\beta_o = \sin \theta_o$, the five curves with the incident angle varying from 0 to 60 degrees coincide almost perfectly, as shown in Fig. 15b.

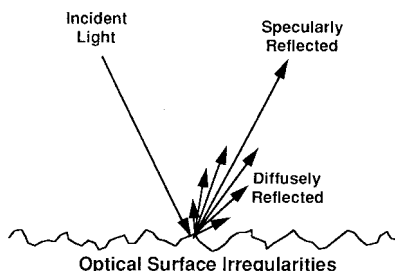


FIGURE 14 Optical surface irregularities produce a specularly reflected beam with a diffusely reflected component that can degrade optical performance in several different ways.

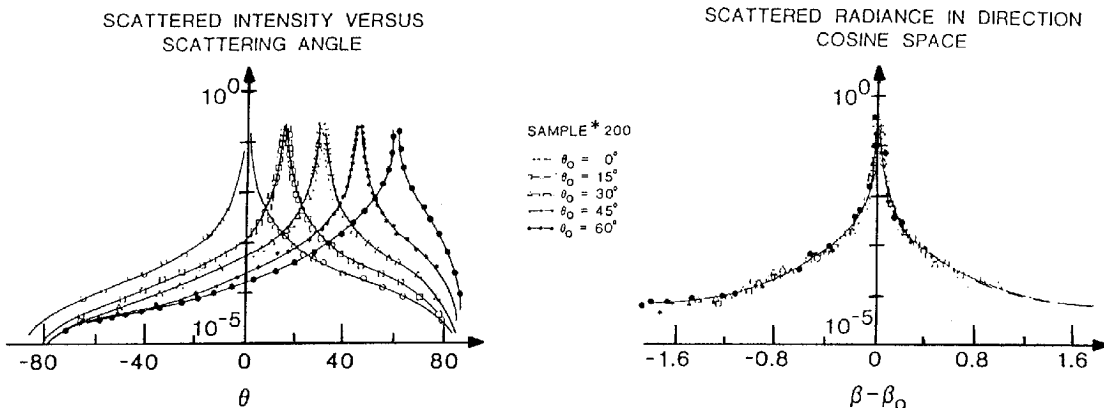


FIGURE 15 (a) Scattered intensity versus scattering angle; (b) scattered radiance in direction cosine space.

Transfer Function Characterization of Scattering Surfaces

The *shift-invariant* scattering behavior shown above implies the existence of a *surface transfer function* which can be shown to relate the scattering properties to the surface characteristics.⁶¹ By describing surface scatter phenomena as a diffraction process in which the rough surface introduces random phase variations into the effective pupil function of the system, an analytical expression can be obtained for the transfer function of the scattering surface. Harvey has shown that if we assume a stationary process (i.e., a random, homogeneous, isotropic mirror surface), and a Gaussian surface height distribution function as shown in Fig. 16, this transfer function is described by the following expression:⁶²

$$H_s(\hat{x}, \hat{y}) = \exp \left\{ -(4\pi\hat{\sigma}_s)^2 \left[1 - \hat{C}_s \left(\frac{\hat{x}}{\hat{l}}, \frac{\hat{y}}{\hat{l}} \right) / \hat{\sigma}_s^2 \right] \right\} \quad (10)$$

This transfer function is described only in terms of the rms surface roughness and the surface autocovariance function and therefore provides a simple solution to the inverse scattering problem. Note that a scaled coordinate system is utilized in which the spatial coordinates are normalized by the wavelength of light; i.e., $\hat{x} = x/\lambda$, $\hat{y} = y/\lambda$, and $\hat{\sigma} = \sigma/\lambda$, etc.

Considerable insight into the scattering process can now be obtained by considering the

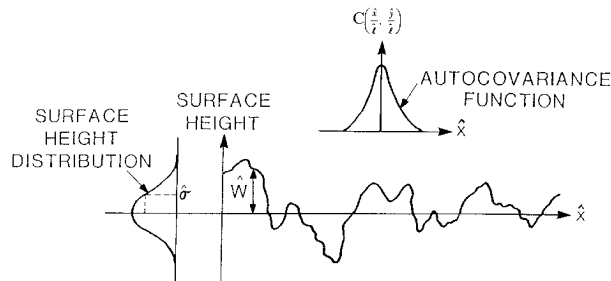


FIGURE 16 A surface profile and the relevant statistical parameters.

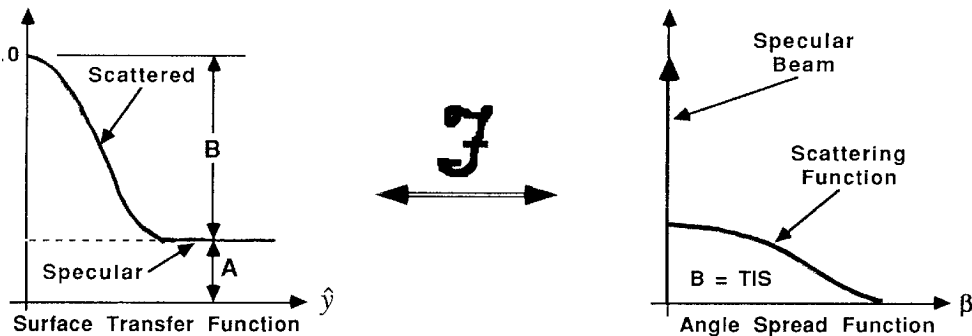


FIGURE 17 (a) The surface transfer function, and (b) the associated angle spread function are related by the Fourier transform operation just as are the optical transfer function (OTF) and the point spread function (PSF) of modern image formation theory.

nature of this transfer function. The autocovariance function approaches the value σ^2 as the displacement approaches zero. The equivalent transfer function thus approaches unity as expected. As the displacement approaches infinity, the autocovariance function approaches zero and the equivalent transfer function approaches a plateau of height $\exp[-(4\pi\hat{\sigma}_s)^2]$. The equivalent transfer function of the scattering surface can thus be regarded as the sum of a constant component and a bell-shaped component as shown in Fig. 17a. Equation (10) can therefore be rewritten as

$$H(\hat{x}, \hat{y}) = A + BQ(\hat{x}, \hat{y}) \quad (11)$$

where

$$A = \exp[-(4\pi\hat{\sigma})^2] \quad (12)$$

$$B = 1 - A = 1 - \exp[-(4\pi\hat{\sigma})^2] \quad (13)$$

$$Q(\hat{x}, \hat{y}) = \frac{\exp\left[(4\pi\hat{\sigma}_s)^2 \hat{C}_s\left(\frac{\hat{x}}{\hat{l}}, \frac{\hat{y}}{\hat{l}}\right) / \hat{\sigma}_s^2\right] - 1}{\exp[-(4\pi\hat{\sigma}_s)^2] - 1} \quad (14)$$

The significance of this interpretation of the equivalent transfer function of the scattering surface is shown by the inferred properties of the corresponding *angle spread function*. Since the transfer function is the sum of two separate components, the angle spread function of the scattering surface is the sum of the Fourier transforms of the two component functions.

$$\mathcal{S}(\alpha, \beta) = \mathcal{F}\{H_s(\hat{x}, \hat{y})\} = A \delta(\alpha, \beta) + S(\alpha, \beta) \quad (15)$$

where \mathcal{F} denotes the Fourier transform operator and the scattering function is given by

$$S(\alpha, \beta) = B \mathcal{F}\{Q(\hat{x}, \hat{y})\} \quad (16)$$

The constant component of the transfer function transforms into a delta function, and the bell-shaped component transforms into a bell-shaped scattering function as illustrated in Fig. 17b. Hence the scattering surface reflects an incident beam of light as a specularly reflected beam of diminished intensity surrounded by a halo of scattered light. Furthermore, from the central ordinate theorem of Fourier transform theory, the relative power distribution between the specular component and the scattered component of the angle spread function are given by the quantities A and B , respectively.

By describing the transfer function in terms of the normalized spatial variables, the

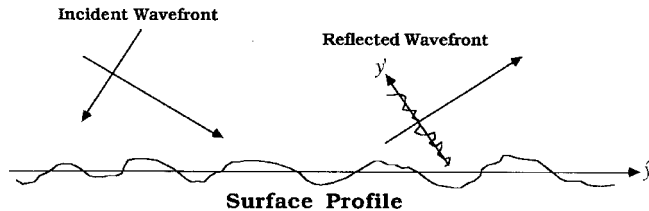


FIGURE 18 Grazing incidence reduces the rms wavefront error induced by the surface irregularities and foreshortens the wavefront features in the plane of incidence.

reciprocal variables in Fourier transform space are the direction cosines of the propagation vectors of the scattered radiation.

Effects of Grazing Incidence. The profile of an optical surface determines the detailed phase front of the reflect wave. At normal incidence, the surface irregularities are merely replicated onto the reflected wavefront with the wavefront error W being twice the surface error. For an arbitrary angle of incidence, this wavefront error is given by $W = 2h \cos \theta$, where h is the surface height deviation and θ is the incident angle measured from the surface normal. The grazing angle ϕ is the complement of the incident angle θ ; hence, the rms wavefront error is

$$\sigma_w = 2\sigma_s \sin \phi \quad (17)$$

where σ_s is the rms surface roughness. There is also a foreshortening of the wavefront features in the plane of incidence by an amount equal to the sine of the grazing angle as illustrated in Fig. 18.

An isotropic surface with a rotationally symmetric surface autocovariance function of width l will thus produce a wavefront autocovariance function which is attenuated by the factor $\sin^2 \phi$ and foreshortened in the plane of incidence by the factor $\sin \phi^{63}$

$$C_W(\hat{x}, \hat{y}) = (4 \sin^2 \phi) C_s \left(\frac{\hat{x}}{\hat{l}}, \frac{\hat{y}}{\hat{l} \sin \phi} \right) \quad (18)$$

The transfer function of a scattering surface at grazing incidence can thus be written as

$$H_s(\hat{x}, \hat{y}) = \exp \left\{ - (4\pi \sin \phi \sigma_s)^2 \left[1 - \hat{C}_s \left(\frac{\hat{x}}{\hat{l}}, \frac{\hat{y}}{\hat{l} \sin \phi} \right) \right] / \hat{\sigma}_s^2 \right\} \quad (19)$$

and the previous expression, Eq. (11), for the surface transfer function in terms of the quantities A and B is still valid:

$$H(\hat{x}, \hat{y}) = A + B Q(\hat{x}, \hat{y}) \quad (20)$$

However, now

$$A = \exp [- (4\pi \sin \phi \hat{\sigma}_s)^2] \quad (21)$$

$$B = 1 - A = 1 - \exp [- (4\pi \sin \phi \hat{\sigma}_s)^2] \quad (22)$$

and

$$Q(\hat{x}, \hat{y}) = \frac{\exp \left[(4\pi \sin \phi \hat{\sigma}_s)^2 \hat{C}_s \left(\frac{\hat{x}}{\hat{l}}, \frac{\hat{y}}{\hat{l} \sin \phi} \right) / \hat{\sigma}_s^2 \right] - 1}{\exp [- (4\pi \sin \phi \hat{\sigma}_s)^2] - 1} \quad (23)$$

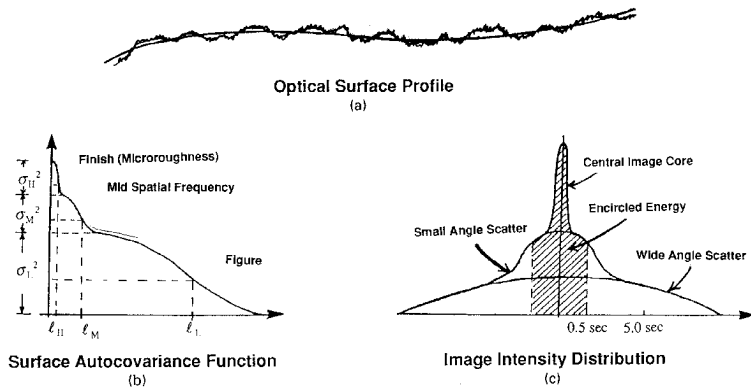


FIGURE 19 (a) Optical surface profile composed of low spatial frequency figure errors, mid spatial frequency surface irregularities, and high spatial frequency microroughness; (b) composite surface autocovariance function; (c) point spread function consisting of a narrow image core, a small-angle scatter function, and a wide-angle scattered halo.

The quantities A and B still correspond to the fraction of the total reflected energy which is contained in the specular beam and the total integrated scatter (TIS), respectively.

Bridging the Gap Between Figure and Finish. It is finally being recognized that residual surface roughness over the *entire range of relevant spatial frequencies* must be specified and controlled in many precision optical systems. This includes the “mid” spatial frequency surface errors that span the gap between the traditional “figure” and “finish” errors.⁶⁴ For many high-resolution grazing incidence x-ray imaging systems, the small-angle scatter due to mid spatial frequency surface ripple is often a dominant source of image degradation.

If we schematically represent a hypothetical optical surface as a low spatial frequency surface figure error overlaid with an uncorrelated mid spatial frequency ripple, which in turn is modulated by a high spatial frequency microroughness as shown in Fig. 19a; we can express the optical fabrication transfer function of this surface as the product of three separate transfer functions representing each of the three spatial frequency regimes

$$H_{\text{fab}} = H_L + H_M + H_H \quad (24)$$

or

$$\begin{aligned} H_{\text{fab}} = & \exp \{ - (4\pi(\sin \phi)\hat{\sigma}_L)^2 [1 - \hat{C}_L/\hat{\sigma}_L^2] \} \\ & \times \exp \{ - (4\pi(\sin \phi)\hat{\sigma}_M)^2 [1 - \hat{C}_M/\hat{\sigma}_M^2] \} \\ & \times \exp \{ - (4\pi(\sin \phi)\hat{\sigma}_H)^2 [1 - \hat{C}_H/\hat{\sigma}_H^2] \} \end{aligned} \quad (25)$$

The expression for the total fabrication transfer function can be simplified by noting that the total surface autocovariance function can be expressed as a sum of the individual autocovariance functions representing the different spatial frequency regimes as illustrated in Fig. 19b

$$C_S = C_L + C_M + C_H \quad (26)$$

The component variances sum to a total surface variance of

$$\sigma_s^2 = \sigma_L^2 + \sigma_M^2 + \sigma_H^2 \quad (27)$$

hence

$$H_{\text{fab}} = \exp \{ - (4\pi(\sin \phi)\hat{\sigma}_s)^2 [1 - \hat{C}_s/\hat{\sigma}_s^2] \} \quad (28)$$

The microroughness will produce a very wide-angle scatter function, the mid spatial frequency ripple will produce a small-angle scatter function, and the low spatial frequency figure error will contribute to the central image core as depicted in Fig. 19c. The shaded portion of the image intensity distribution represents the fractional encircled energy.

A requirement on fractional encircled energy is widely used as a specification on image quality. Since most x-ray/EUV imaging systems are far from diffraction-limited, the image core is usually completely contained within the specified circled. Virtually all the radiation scattered at wide angles due to microroughness falls outside the specified circle. However, the small-angle scatter distribution due to mid spatial frequency surface errors may have a width comparable to the specified circle diameter. Hence, the fractional encircled energy will be quite sensitive to both the amplitude and spatial frequency of the optical surface errors in this intermediate domain between the traditional surface figure and surface finish.

Short-wavelength Considerations. At these very short x-ray wavelengths, the smooth-surface approximation is frequently not valid, and conventional perturbation techniques cannot always be used for calculating the effects of scatter due to residual optical fabrication errors. It is important that we thoroughly understand the relationship between these surface characteristics and the associated image degradation.

The transfer function characterization of scattering surfaces expressed by Eq. (10) was based upon a scalar diffraction formulation; however, no explicit smooth surface approximation has been made. As illustrated in Fig. 20, the Fourier transform of the surface autocovariance function is the surface power spectrum or power spectral density (PSD) function. The image characteristics (generalized point spread function) are related to the complex pupil function in exactly the same way as the surface PSD is related to the surface profile.

$$P(\hat{x}, \hat{y}) = A(\hat{x}, \hat{y}) \exp [2\pi\hat{W}(\hat{x}, \hat{y})], \quad \hat{W}(\hat{x}, \hat{y}) = 2(\sin \phi)\hat{h}(\hat{x}, \hat{y}) \quad (29)$$

The surface transfer function, expressed previously in Eq. (28), becomes one term of the system optical transfer function (OTF). The other term is the conventional OTF representing the effects that determine the width of the image core (diffraction, aberrations, misalignments, environmental errors, etc.)

$$H(\hat{x}, \hat{y}) = H_c(\hat{x}, \hat{y})H_{\text{fab}}(\hat{x}, \hat{y}) \quad (30)$$

SURFACE CHARACTERISTICS IMAGE CHARACTERISTICS

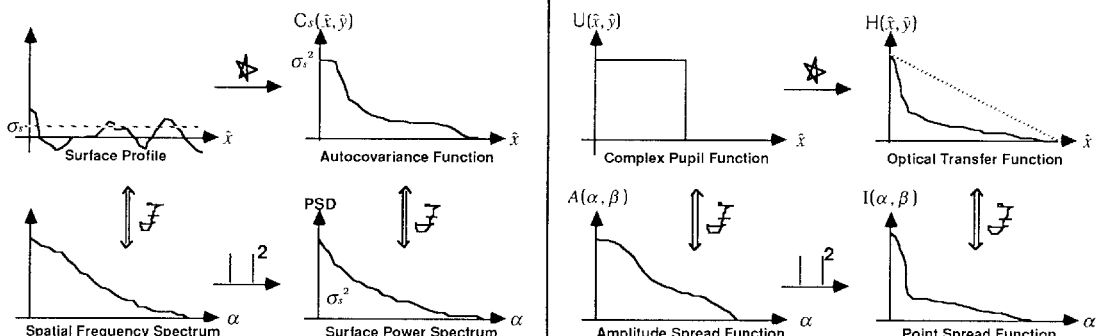


FIGURE 20 The point spread function of an imaging system is related to the complex pupil function in exactly the same way that the surface PSD is related to the surface profile.

The generalized point spread function will thus be given by convolving this image core with the angle spread function discussed earlier in Eq. (15)

$$I(\alpha, \beta) = I_c(\alpha, \beta) * \mathcal{S}(\alpha, \beta) \quad (31)$$

It should again be emphasized that the smooth surface approximation is generally not valid at these very short wavelengths; however, if we do assume that $\hat{\sigma} \ll 1$, the specular reflectance is given by

$$A \approx 1 - (4\pi\hat{\sigma}_s)^2 \quad (32)$$

the total integrated scatter (TIS) is given by

$$B \approx (4\pi\hat{\sigma}_s)^2 \quad (33)$$

and the function $Q(\hat{x}, \hat{y})$ reduces to the normalized surface autocovariance function

$$Q(\hat{x}, \hat{y}) \approx \hat{C}_s \left(\frac{\hat{x}}{\hat{l}}, \frac{\hat{y}}{\hat{l}} \right) / \hat{\sigma}_s^2 \quad (34)$$

This results in the often quoted and widely used statement that the scattering function is directly proportional to the surface power spectral density (PSD) function.^{65,66}

$$S(\alpha, \beta) = \text{scattering function} = B \mathcal{F}\{Q(\hat{x}, \hat{y})\} = (4\pi/\lambda)^2 \text{PSD} \quad (35)$$

However, one must remember that this is only true when the smooth surface approximation is valid, and even for the best optical surfaces available, this is frequently not the case when dealing with x-ray/EUV radiation.

Multilayer Scattering Characteristics

It is widely recognized that scatter effects from interface microroughness can decimate the reflectance of multilayer coatings in normal-incidence soft x-ray imaging systems.⁶⁷⁻⁷¹ The (spectral) reflectance has thus become the most common measure of performance in the evaluation of x-ray multilayers. However, high x-ray reflectance is a necessary but not sufficient condition for producing high-quality images. A second and equally important condition is the ability to concentrate the reflected radiation in a very small region in the focal plane. We will proceed to describe the concept of an enhanced reflectance multilayer as a low-pass spatial frequency filter acting upon the substrate PSD. This concept allows us to apply conventional linear systems techniques to the evaluation of image quality, and to the derivation of optical fabrication tolerances, for applications utilizing multilayer coatings.

The reflectance, at normal incidence, from a single interface can be calculated using the following Fresnel reflectance formula, if the refractive indices of the respective media separated by the interface are known.

$$R = |r|^2 = (n_2 - n_1)^2 / (n_2 + n_1)^2 \quad (36)$$

This value for reflectance is valid whether the interface is rough or not. In the case of a rough interface, the reflected wavefront takes on a disturbance of the same form as the interface but of twice the amplitude. As a result, some fraction of the light will be scattered away from the specular direction. We represent this fact by writing the specularly reflected power as

$$P_s = RAP_o \quad (37)$$

and the diffusely scattered power as

$$P_d = RBP_o \quad (38)$$

where R is the Fresnel reflectance, P_o is the incident power, and A and B are again given by

$$A = \exp [- (4\pi\sigma/\lambda)^2] \quad (39)$$

and

$$B = \text{total integrated scatter} = 1 - A \quad (40)$$

and are the fraction of reflected power in the specular and scattered beams, respectively. Here σ is the rms surface roughness over the entire range of relevant spatial frequencies, from high spatial frequency microroughness, through mid spatial frequency surface irregularities, and including low spatial frequency figure errors

$$\sigma^2 = \sigma_L^2 + \sigma_M^2 + \sigma_H^2 \quad (41)$$

Similarly, the radiation reflected by an enhanced reflectance multilayer will consist of a specular and diffuse part as shown in Fig. 21. The specularly reflected and diffusely reflected components are still given by equations of the form of Eqs. (37) and (38); however, the relative strength of the specular beam will now depend upon the *effective* roughness, σ' , which in turn depends upon the degree of *correlation* between the various interfaces. Hence, for the multilayer

$$A' = \exp [- (4\pi\sigma'/\lambda)^2] \quad (42)$$

and

$$B' = \text{total integrated scatter} = 1 - A' \quad (43)$$

where

$$\sigma'^2 = \sigma'_L^2 + \sigma'_M^2 + \sigma'_H^2 \quad (44)$$

Eastman (1974), Carniglia (1979), Elson (1980), and Amra (1991) have also contributed to our understanding of scattering from optical surfaces with multilayer coatings.⁷²⁻⁷⁵ However, in most cases they have dealt only with microroughness and have assumed that the interfaces are either perfectly correlated or perfectly uncorrelated.

We are considering the surface irregularities over the entire range of relevant spatial frequencies from the very low spatial frequency *figure* errors to the very high spatial

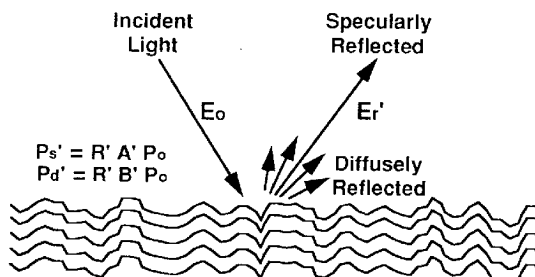


FIGURE 21 An enhanced reflectance multilayer also produces a specularly reflected beam and a diffusely reflected component whose relative strengths depend upon the degree of correlation between the various interfaces.

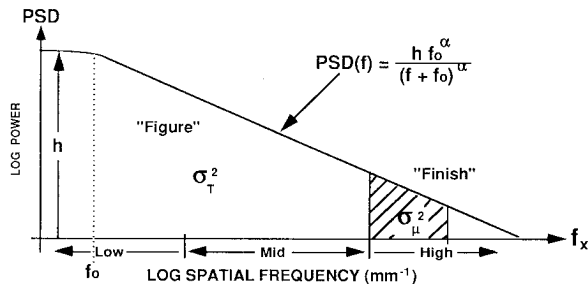


FIGURE 22 The substrate surface PSD is assumed to obey an inverse power law which spans the entire range of spatial frequencies from low spatial frequency *figure* errors to high spatial frequency *finish*.

frequency *finish* errors. It therefore seems rather intuitive that for any reasonable thin-film deposition process, the low spatial frequency figure errors will *print through* and be correlated from layer to layer, while the high spatial frequency microroughness inherent to the deposition process itself will be uncorrelated from layer to layer. Let us assume that each interface making up the multilayer has the same surface statistics.

Let us also assume that the interfaces can be characterized by an inverse power law surface PSD as illustrated in Fig. 22.

Note that this is a radial profile of a two-dimensional PSD plotted as log power expressed in waves squared per spatial frequency squared versus log spatial frequency. The units are thus consistent with a volume under the PSD of σ^2 as required. The low, mid, and high spatial frequency domains are indicated in Fig. 22. Furthermore, knowing the functional form of the surface PSD now enables one to calculate the total rms surface error σ from a band-limited measurement of the microroughness σ_μ with an instrument such as a micro phase-measuring interferometer.

It has been pointed out by Spiller that spatially uncorrelated microroughness in x-ray/EUV multilayers will yield an effective rms surface roughness reduced by a factor of $1/\sqrt{N}$, where N is the number of layer pairs.⁶⁹ From this and the knowledge that the interfaces will be highly correlated at mid and low spatial frequencies, it is clear that the multilayer will act as a low-pass spatial frequency filter which has a value of unity for correlated low spatial frequencies and drops to a value of $1/N$ for uncorrelated high spatial frequencies. The exact location and shape of this cutoff depends upon the material and deposition process. However, the PSD filter function is illustrated qualitatively in Fig. 23.

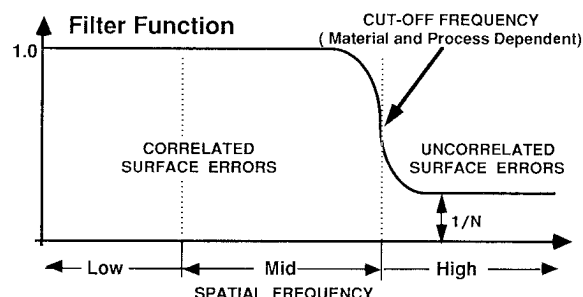


FIGURE 23 Enhanced reflectance multilayer coatings behave as a low-pass spatial frequency filter acting upon the interface PSD.

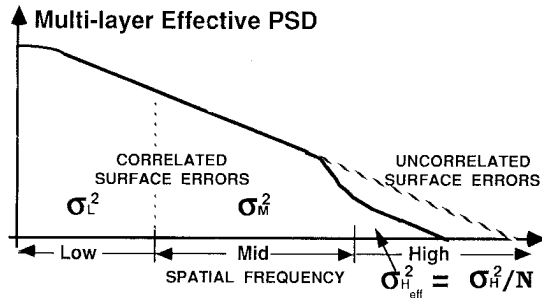


FIGURE 24 The filtered interface PSD is the effective PSD of the multilayer.

Figure 24 illustrates the effective multilayer PSD obtained by multiplying the interface PSD by the multilayer filter function. Note that the effective microroughness (and hence the wide-angle scatter) has been substantially reduced.

This effective PSD of the multilayer completely characterizes the scattering effects which degrade the image quality of normal-incidence x-ray imaging systems.

Other useful references dealing with surface scatter for general optical applications include *Introduction to Surface Roughness and Scattering* by J. M. Bennett and L. Mattsson,⁷⁶ *Optical Scattering, Measurement and Analysis* by John C. Stover,⁷⁷ and a myriad of excellent papers published over the years by Eugene Church.⁷⁸⁻⁸⁵

11.8 IMAGE QUALITY PREDICTIONS FOR VARIOUS APPLICATIONS

A scalar diffraction treatment of surface scatter phenomena can now be used to make image quality predictions as degraded by residual optical fabrication errors. The effective PSD (including the effects of multilayer scattering) can be Fourier transformed to obtain the effective surface autocovariance function. This effective surface autocovariance function can be substituted into Eq. (28) to obtain the transfer function of the scattering surface. The product of this surface transfer function and the conventional optical transfer function describing the effects of diffraction, geometrical aberrations, misalignments, etc. can then be Fourier transformed to obtain a generalized point spread function including the effects of scattering.⁸⁶

In the absence of good metrology data, parametric calculations can be made to determine the performance sensitivity to assumed optical fabrication tolerances and to wavelength. In fact, these parametric curves can be used to derive the optical fabrication tolerances necessary for a given application. A few examples follow.

Extreme Ultraviolet (EUV) Astronomy

NASA's Far Ultraviolet Spectroscopic Explorer (FUSE) telescope design is the Wolter Type II grazing incidence configuration shown in Fig. 25. The FUSE program requires a fractional encircled energy of 0.5 in a 1.0 arcsec diameter circle from an on-axis point source with a wavelength of 1000 Å. Figure 26 illustrates the severe image degradation that would occur in the 100- to 350-Å EUV region of the electromagnetic spectrum for optical fabrication tolerances chosen to meet the above requirement.⁸⁷ The scattering theory discussed in the previous section of this chapter has been used to make exhaustive image

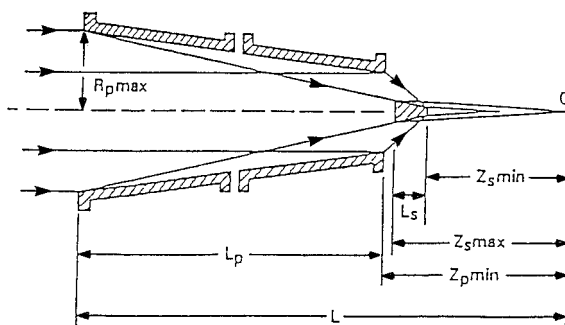


FIGURE 25 Schematic illustration of the FUSE telescope design.

quality predictions as a function of various optical surface parameters. The resulting sensitivity curves were used to determine the optical fabrication tolerances necessary to achieve considerably enhanced EUV performance.⁸⁸ These parametric performance predictions can then be used as the basis of a detailed cost versus performance trade study.

High Energy X-ray Astrophysics with Conical Foil X-ray Telescopes

Scientists at the Danish Space Research Institute (DSRI) are currently fabricating and testing conical foil grazing incidence mirrors for the XSPECT telescope being developed for the Soviet Spectrum-X-Gamma mission.³⁰ This telescope will have 154 concentric shells with grazing angles varying from 9 to 33 arcmin. Image degradation due to diffraction effects and geometrical aberrations caused by the conical shape of these mirrors were discussed previously in this chapter; however, detailed image quality predictions indicate that scattering effects and alignment errors will limit the achievable resolution to

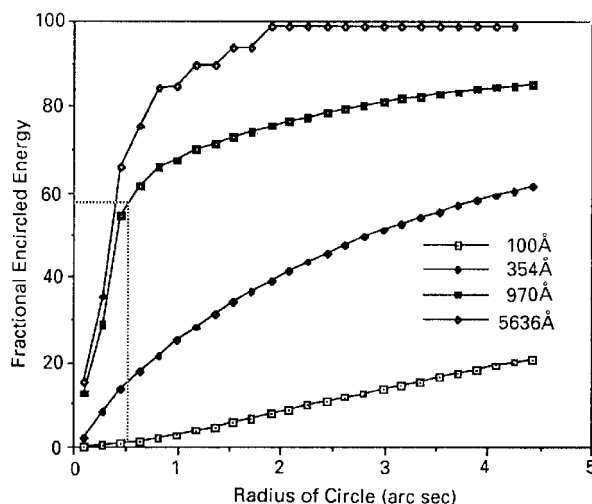


FIGURE 26 Fractional encircled energy at different wavelengths including optical fabrication and alignment errors.

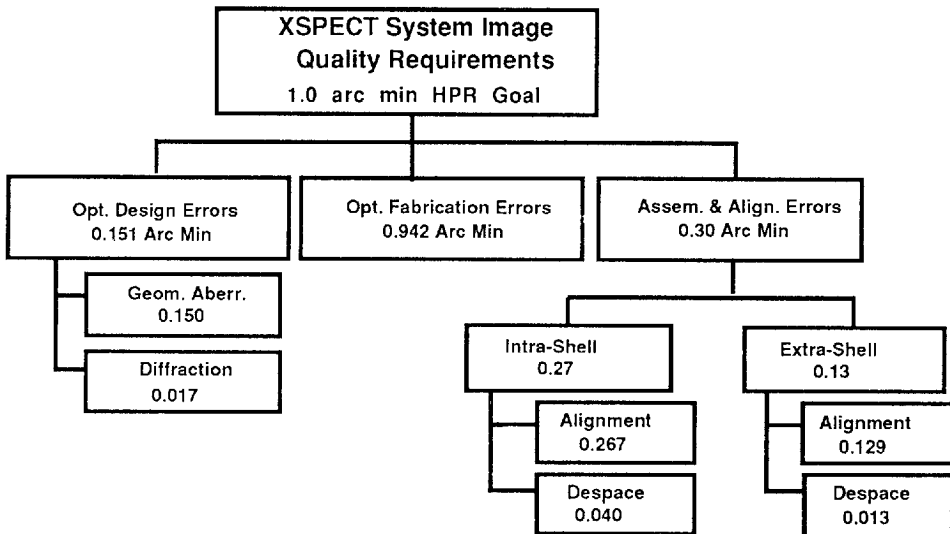


FIGURE 27 XSPECT system error budget.

approximately two minutes of arc.⁸⁹ Figure 27 shows an error budget tree that illustrates the relative contributions of the various error sources for x-ray telescopes of this type. Note that scattering effects from optical fabrication errors are by far the dominant error source.

X-ray Solar Physics

Figure 28 illustrates fractional encircled energy predictions for the Stanford/MSFC normal-incidence Cassegrain solar telescope reported to have a resolution of approximately 1.0 arcsec.⁴⁸ In order to obtain super-smooth surfaces, spherical mirrors were used rather than the paraboloid and hyperboloid of a classical Cassegrain configuration. This

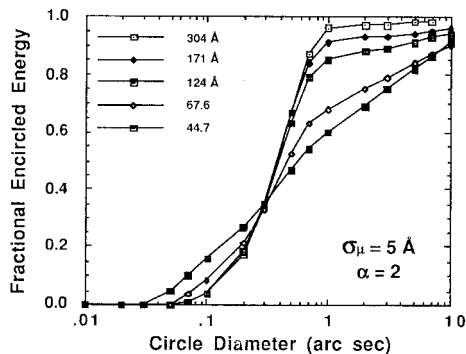


FIGURE 28 Encircled energy predictions for the Stanford/MSFC Cassegrain X-ray Solar Telescope. A surface PSD obeying an inverse-square law and a band-limited microroughness of 5 \AA were assumed.

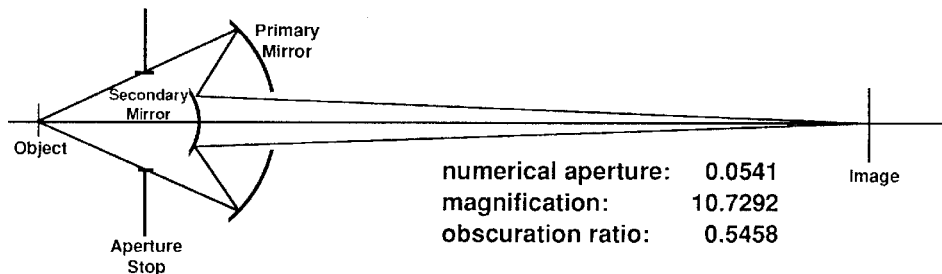


FIGURE 29 Schwarzschild soft x-ray microscope configuration.

resulted in a significant amount of spherical aberration. Note that our predictions indicate a fractional encircled energy of 0.9 in a 1.0-arcsec circle at the operational wavelength of 171 Å, which is in good agreement with the experimental data. However, parametric performance predictions indicate that current optical fabrication technology for aspheric surfaces will not allow the order-of-magnitude improvement projected by the Stanford/MSFC group.⁹⁰

Soft X-ray Microscopy

The Schwarzschild microscope configuration consists of two concentric spherical mirrors with an aperture stop at their common center of curvature as shown in Fig. 29.

The curves in Fig. 30 illustrate the predicted optical performance of this Schwarzschild microscope with state-of-the-art surfaces at the soft x-ray wavelengths of 300 Å, 130 Å, and 50 Å. For general microscopy applications where fine details in extended objects are being studied, some property of the modulation transfer function (MTF) is probably the most appropriate image quality criterion. Let us assume that a modulation of 0.20 is just acceptable for our application. Image plane *resolution* will thus be defined as the reciprocal of the spatial frequency at which the modulation drops to a value of 0.20 and

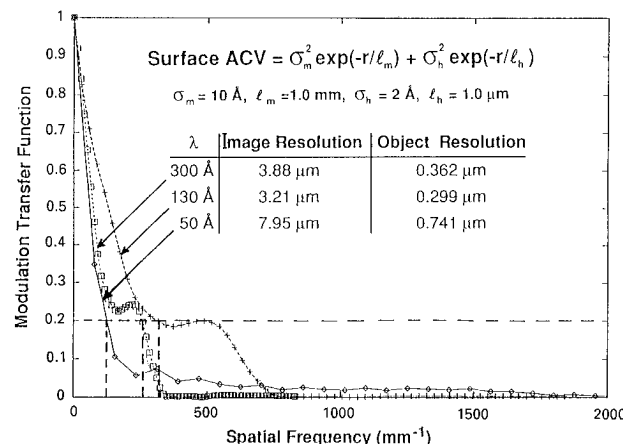


FIGURE 30 Performance sensitivity of a Schwarzschild soft x-ray microscope upon surface scatter effects due to mid spatial frequency optical fabrication errors.

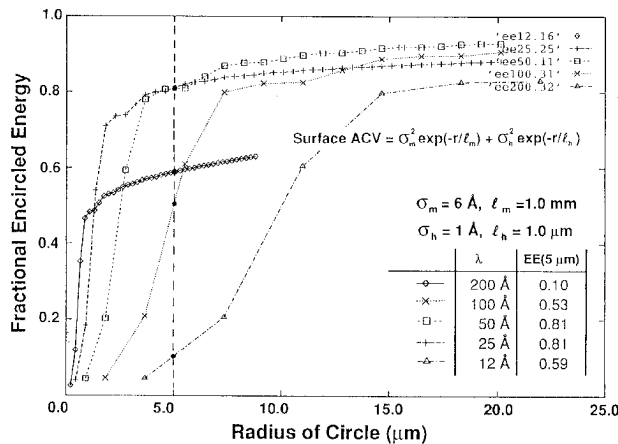


FIGURE 31 Fractional encircled energy of a soft x-ray synchrotron beamline consisting of five grazing incidence mirrors with state-of-the-art fabrication tolerances.

the object plane resolution is this number divided by the microscope magnification. Note that the intermediate wavelength has the best resolution. The long wavelength (300 \AA) resolution is limited by diffraction with negligible degradation from scattering. At 130 \AA there is a modest 16 percent degradation in the object resolution due to scattering. And at 50 \AA , mid spatial frequency scattering effects are by far the dominant image degradation mechanism, with the smallest resolvable object 12 times as large as the diffraction-limited value.⁹¹ Clearly, high resolution soft x-ray microscopy of biological specimens in the water window ($25 \text{ \AA} < \lambda < 50 \text{ \AA}$) will require ultrasmooth (rms microroughness $< 1 \text{ \AA}$) surfaces.

Detailed analysis has shown that a $0.1\text{-}\mu\text{m}$ object resolution with a $1.0\text{-}\mu\text{m}$ depth-of-field over an $850\text{-}\mu\text{m}$ object field diameter can be obtained at a wavelength of 43 \AA with a Schwarzschild microscope configuration. This includes the effects of geometric aberrations, assembly and alignment errors, diffraction effects, and scattering effects from optical fabrication errors.⁹²

X-ray Synchrotron Source Applications

Figure 31 illustrates the predicted performance of a soft x-ray synchrotron beamline consisting of five grazing incidence mirrors ($\alpha = 3^\circ$) with state-of-the-art optical fabrication tolerances. We have chosen fractional encircled energy in a $5\text{-}\mu\text{m}$ radius circle (corresponds to a $10\text{-}\mu\text{m}$ monochrometer slit width) as our image quality criterion. Again we see that diffraction dominates image degradation at the long wavelengths ($\lambda > 100 \text{ \AA}$), and scattering dominates image degradation at the short wavelength ($\lambda = 12 \text{ \AA}$). The best performance is obtained for intermediate wavelengths ($25 \text{ \AA} > \lambda > 50 \text{ \AA}$).⁹³

11.9 SUMMARY AND CONCLUSIONS

We first reviewed recent progress in both grazing incidence x-ray imaging systems and the rapidly emerging technology of enhanced reflectance x-ray multilayers. Four specific potential pitfalls in the design and analysis of x-ray/EUV imaging systems were then

identified. These included: (1) assuming negligible diffraction effects at x-ray wavelengths; (2) overlooking the effects of ghost images in grazing incidence x-ray/EUV imaging systems; (3) assuming that residual design errors dominate optical fabrication errors at these very short wavelengths; and (4) assuming that high reflectance implies negligible scattering in x-ray multilayers. The importance of utilizing a systems engineering approach and an exhaustive error budget analysis was also emphasized.

The diffraction behavior of highly obscured annular apertures was shown to offset the popular notion that diffraction effects are negligible at short wavelengths.

Grazing incidence imaging systems are particularly difficult to control stray radiation from out-of-field sources. Ghost image behavior in Wolter Type I telescopes was discussed in detail.

It was then emphasized that, even our best optical surfaces are not always “smooth” relative to these very short wavelengths. Image degradation due to scattering effects from surface irregularities in several different spatial frequency regimes was discussed. Small angle scatter from mid-spatial frequency optical fabrication errors that bridge the gap between traditional figure and finish errors were shown to dominate residual design errors in several x-ray/EUV imaging applications of interest. X-ray multilayers were shown to behave as a surface PSD filter function which can conveniently be used to predict image degradation due to interface roughness. Uncorrelated microroughness in x-ray multilayers decimates reflectance but does not significantly degrade image quality.

Finally, parametric image quality predictions for a variety of applications including x-ray/EUV astronomy, soft x-ray microscopy, soft x-ray microlithography, and x-ray synchrotron beamline mirrors were presented to demonstrate the wavelength dependence of optical fabrication tolerances for x-ray imaging systems.

11.10 REFERENCES

1. N. M. Ceglio, “Revolution in X-ray Optics,” *J. X-ray Sci. and Tech.* **1**:7–78 (1989).
2. V. Rehn, “Grazing Incidence Optics for Synchrotron Radiation Insertion-device Beams,” *Proc. SPIE* **640**:106–115 (1986).
3. H. Rarback et al., “Coherent Radiation for X-ray Imaging—The Soft X-ray Undulator and the X1A Beamline at the NSLS,” *J. X-ray Sci. and Tech.* **2**:274–296 (1990).
4. D. R. Gabardi and D. L. Shealy, “Optical Analysis of Grazing Incidence Ring Resonators for Free-electron Lasers,” *Opt. Eng.* **29**:641–648 (1990).
5. A. G. Michette, “Laser-generated Plasmas: Source Requirements for X-ray Microscopy,” *J. X-ray Sci. and Tech.* **2**:1–16 (1990).
6. T. W. Barbee, Jr., “Multilayers for X-ray Optics,” *Opt. Eng.* **25**:898–915 (1986).
7. J. F. Osantowski and L. Van Speybroeck (eds.), Twenty-three Papers Presented at the 1986 SPIE Conference “Grazing Incidence Optics,” *Proc. SPIE* **640** (1986).
8. Fourteen Papers on X-ray/EUV Optics in a Special Issue of Optical Engineering, *Opt. Eng.*, **29**:576–671 (June 1990).
9. Eleven Papers on X-ray/EUV Optics in a Special Issue of Optical Engineering, *Opt. Eng.*, **29**:698–780 (July 1990).
10. R. B. Hoover (ed.), Seventy-one Papers Presented at the 1989 SPIE Conference “X-ray/EUV Optics for Astronomy and Microscopy,” *Proc. SPIE* **1160** (1989).
11. J. Boker (ed.), Thirty-four Papers Presented at a Symposium on “Soft X-ray Projection Lithography,” *Proc. OSA* **12** (1991).
12. P. Kirkpatrick and A. V. Baez, “Formation of Optical Images by X-rays,” *J. Opt. Soc. Am.* **38**:776 (1948).
13. H. Wolter, “Spiegelsysteme streifenden Einfalls als abbildende Optiken für Röntgenstrahlen,” *Ann. Phys.*, NY **10**:94 (1952).

14. B. Aschenbach, "X-ray Telescopes," *Rep. Prog. Phys.*, **48**:579–629 (1985).
15. L. P. Van Speybroeck, "Grazing Incidence Optics for the U.S. High-resolution X-ray Astronomy Program," *Opt. Eng.* **27**:1398–1403 (1988).
16. A. Slomba, R. Babisch, and P. Glenn, "Mirror Surface Metrology and Polishing for AXAF/TMA," *Proc. SPIE* **597**:40 (1985).
17. B. Aschenbach, "Design, Construction, and Performance of the ROSAT High-resolution Mirror Assembly," *Appl. Opt.* **27**:1404–1413 (1988).
18. R. Giacconi et al., "The Einstein (HEAO 2) X-ray Observatory," *Astrophys. J.* **230**:540 (1979).
19. L. P. Van Speybroeck, "Einstein Observatory (HEAO B) Mirror Design and Performance," *Proc. SPIE* **184**:2 (1979).
20. L. P. Van Speybroeck, P. Reid, D. Schwartz, and J. Bilbro, "Predicted and Preliminary Evaluation of the X-ray Performance of the ACAF Technology Mirror Assembly," *Proc. SPIE* **1160**:94 (1989).
21. M. V. Zombeck, "Advanced X-ray Astrophysics Facility (AXAF)-Performance Requirements and Design Considerations", *Proc. SPIE*, **184** (1979).
22. J. E. Harvey, "Recent Progress in X-ray Imaging", presented at the *AIAA Space Programs and Technologies Conference* in Huntsville, AL (Sept. 1990).
23. T. T. Saha, D. A. Thomas, and J. F. Osantowski, "OSAC Analysis of the Far Ultraviolet Explorer (FUSE) Telescope," *Proc. SPIE* **640**:79–84 (1986).
24. C. B. Zarowin, "A Theory of Plasma-assisted Chemical Vapor Transport Processes," *J. Appl. Phys.* **57**(3):929–942 (1985).
25. S. Bowyer and J. Green, "Fabrication, Evaluation, and Performance of Machined Metal Grazing Incidence Telescopes," *Appl. Opt.* **27**:1414–1422 (1988).
26. R. C. Catura, E. G. Joki, D. T. Roethig, and W. J. Brookover, "Lacquer Coated X-ray Optics," *Proc. SPIE* **640**:140–144 (1986).
27. J. A. Nousek et al., "Diamond-turned Lacquer-coated Soft X-ray Telescope Mirrors," *Appl. Opt.* **27**:1430–1432 (1988).
28. R. Petre and P. J. Serlemitsos, "Conical Imaging Mirrors for High-speed X-ray Telescopes," *Appl. Opt.* **24**:1833 (1985).
29. R. Petre, P. J. Serlemitsos, F. E. Marshall, K. Jahoda, and H. Kunieda, "In Flight Performance of the Broad-Band X-ray Telescope," *Proc. SPIE* **1546**:72–81 (1991).
30. N. J. Westergaard, B. P. Byrnak, F. E. Christensen, P. Grundsoe, A. Hornstrup, S. Henrichsen, U. Henrichsen, E. Jespersen, H. U. Norgaard-Nielsen, and J. Polny, "Status of the Development of a Thin Foil High Throughput X-ray Telescope for the Soviet Spectrum X-gamma Mission," *Proc. SPIE* **1160**:488–499 (1989).
31. Y. Tanaka and F. Makino, "Grazing Incidence Optics for the X-ray Astronomy Mission SXO," *Proc. SPIE* **830**:242 (1987).
32. Y. Matsui, M. P. Ulmer, and P. Z. Takacs, "X-ray and Optical Profiler Analysis of Electroformed X-ray Optics," *Appl. Opt.* **27**:1558–1563 (1988).
33. O. Citterio, et al., "Optics for the X-ray Imaging Concentrators Aboard the X-ray Astronomy Satellite SAX," *Proc. SPIE* **830**:139 (1987).
34. W. Egle, H. Bulla, P. Kaufmann, B. Aschenbach, and H. Brauninger, "Production of the First Mirror Shell for ESA's XMM Telescope by Application of a Dedicated Large Area Replication Technique," *Opt. Eng.* **29**:1267 (1990).
35. J. Du Mond and J. P. Youtz, "Selective X-ray Diffraction from Artificially Stratified Metal Films Deposited by Evaporation," *Phys. Rev.* **48**:703 (1935).
36. J. Du Mond and J. P. Youtz, "An X-ray Method for Determining Rates of Diffusion in the Solid State," *J. Appl. Phys.* **11**:357 (1940).
37. J. Dinklage and R. Frerichs, "X-ray Diffraction and Diffusion in Metal Film Layered Structures," *J. Appl. Phys.* **34**:2633 (1963).

38. J. Dinklage, "X-ray Diffraction by Multilayered Thin Film Structures and Their Diffusion," *J. Appl. Phys.* **38**:3781 (1967).
39. E. Spiller, "Low-loss Reflection Coatings Using Absorbing Materials," *Appl. Phys. Lett.* **20**:365 (1972).
40. E. Spiller, "Multilayer Interference Coatings for the Vacuum Ultraviolet," in Proc. ICO-IX, *Space Optics*, p. 525, Natl. Acad. Science, Washington, D.C. (1974).
41. E. Spiller, "Reflective Multilayer Coatings in the Far UV Region," *Appl. Opt.* **15**:2333 (1976).
42. T. W. Barbee, Jr. and D. L. Kieth, "Synthetic Structures Layered on the Atomic Scale," H. Winick and G. Brown (eds.), in Workshop on *X-ray Instrumentation for Synchrotron Radiation Research*, p. III-26, Stanford SSRL Report 7804 (1978).
43. Ten Papers on X-ray Multilayered Optics in a Special Issue of Optical Engineering, *Opt. Eng.* **25**:897-978 (August 1986).
44. G. F. Marshall (ed.), Forty-eight Papers Presented at the 1985 SPIE Conference "Applications of Thin-film Multilayered Structures to Figured X-ray Optics," *Proc. SPIE* **563** (1985).
45. F. E. Christensen (ed.), Thirty-three Papers Presented at the 1988 SPIE Conference on "X-ray Multilayers for Diffractometers, Monochromators, and Spectrometers," *Proc. SPIE* **984** (1988).
46. R. B. Hoover (ed.), Twenty-three Papers Presented at the 1989 SPIE Conference on "X-ray/EUV Optics for Astronomy and Microscopy," *Proc. SPIE* **1160** (1989).
47. N. M. Ceglio (ed.), Thirty-one papers presented at the 1991 SPIE Conference on "Multilayer Optics for Advanced X-ray Applications," *Proc. SPIE* **1547** (1991).
48. A. B. C. Walker, Jr., T. W. Barbee, Jr., R. B. Hoover, and J. F. Lindblom, "Soft X-ray Images of the Solar Corona with a Normal-Incidence Cassegrain Multilayer Telescope," *Science*, vol. 241:1781 (Sept. 1988).
49. W. J. Smith, *Modern Optical Engineering*, 2nd ed., McGraw-Hill, New York, 1990.
50. J. W. Goodman, *Introduction to Fourier Optics*, McGraw-Hill, New York, 1968.
51. J. E. Harvey, "Diffraction Effects in Grazing Incidence X-ray Telescopes," *J. X-ray Sci. and Tech.* **3**:68-76 (1991).
52. H. F. A. Tschunko, "Imaging Performance of Annular Apertures," *Appl. Opt.* **13**:1820 (1974).
53. W. Werner, "Imaging Properties of Wolter I Type X-ray Telescopes," *Appl. Opt.* **16**:764 (1977).
54. C. E. Winkler and D. Korsch, "Primary Aberrations for Grazing Incidence," *Appl. Opt.* **16**:2464 (1977).
55. United Technologies Research Center, *AXAF Technology Briefing*, NASA/MSFC, August 7, 1984.
56. D. Korsch, "Near Anastigmatic Grazing Incidence Telescope," *Proc. SPIE* **493** (1984).
57. M. V. Zombeck, "AXAF Effective Area Studies," *SAO-AXAF-83-015* (1983).
58. E. C. Moran and J. E. Harvey, "Ghost Image Behavior in Wolter Type I X-ray Telescopes," *Appl. Opt.* **27**:1486 (15 April 1988).
59. E. C. Moran, J. E. Harvey, F. E. Christensen, N. J. Westergaard, H. W. Schnopper, B. P. Byrnak, and H. U. Noergaard-Nielsen, "Ghost Image Analysis for XSPEC High-throughput X-ray Telescope Mission," presented at the *173rd Meeting of the American Astronomical Society* in Boston, MA (Jan. 1989).
60. J. D. Mangus, "Strategy and Calculations for the Design of Baffles for Wolter Type II telescopes," *Proc. SPIE* **830**:245-253 (1987).
61. J. E. Harvey, "Surface Scatter Phenomena: a Linear, Shift-invariant Process," *Proc. SPIE* **1165**:87-99 (1989).
62. J. E. Harvey, "Light-Scattering Characteristics of Optical Surfaces," Ph.D. Dissertation, Univ. Arizona (1976).
63. J. E. Harvey, E. C. Moran, and W. P. Zmek, "Transfer Function Characterization of Grazing Incidence Optical Systems," *Appl. Opt.* **27**:1527-1533 (1988).
64. R. J. Noll, "Effect of Mid and High Spatial Frequencies on Optical Performance," *Opt. Eng.* **18**:137 (1979).

65. J. C. Stover, "Roughness Characterization of Smooth Machined Surfaces by Light Scattering," *Appl. Opt.* **14**:1796 (1975).
66. E. L. Church, H. A. Henkinson, and J. M. Zavada, "Relationship Between Surface Scattering and Microtopographic Features," *Opt. Eng.* **18**:125 (1979).
67. J. H. Underwood, T. W. Barbee, and D. L. Shealy, "X-ray and Extreme Ultraviolet Imaging Using Layered Synthetic Microstructures," *SPIE* vol. 316, High Res. Soft X-ray Optics (1981).
68. A. E. Rosenbluth and J. M. Forsyth, "The Reflecting Properties of Soft X-Ray Multilayers," *SPIE*, vol. 563, Applications of Thin-Film Multilayered Structures to Figured X-Ray Optics, 284 (1985).
69. E. Spiller and A. E. Rosenbluth, "Determination of Thickness Errors and Boundary Roughness from the Measured Performance of a Multilayer Coating," *Opt. Eng.* **25**:898 (1986).
70. D. L. Windt and R. C. Catura, "Multilayer Characterization at LPARL," *SPIE*, vol. 984, X-ray Multilayers for Diffractometers, Monochrometers, and Spectrometers, 82 (Aug. 1988).
71. D. G. Stearns, "The Scattering of X-rays from Nonideal Multilayer Structures," *J. Appl. Phys.* **65**(2):498 (15 Jan. 1989).
72. J. M. Eastman, "Surface Scattering in Optical Interface Coatings," Ph.D. dissertation, Univ. of Rochester, Rochester, NY (1974). (Available from University Microfilms, Ann Arbor, MI 48106.)
73. C. K. Carniglia, "Scalar Scattering Theory for Multilayer Optical Coatings," *Opt. Eng.* **18**:104 (1979).
74. J. M. Elson, J. P. Rahn, and J. M. Bennett, "Light Scattering from Multilayer Optics; Comparison of Theory and Experiment," *Appl. Opt.* **19**:669 (1980).
75. C. Amra, J. H. Apfel, and E. Pelletier, "The Role of Interface Correlation in Light Scattering by a Multilayer," *Appl. Opt.* **31**:3134–3151 (1992).
76. J. M. Bennett and L. Mattsson, *Introduction to Surface Roughness and Scattering*, Opt. Soc. of Am., Washington, D.C., 1989.
77. J. C. Stover, *Optical Scattering, Measurement and Analysis*, McGraw-Hill, New York, 1990.
78. E. L. Church, "The Role of Surface Topography in X-ray Scattering," *Proc. SPIE* **184**:196 (1979).
79. E. L. Church, "Small-Angle Scattering from Smooth Surfaces," *J. Opt. Soc. Am.* **70**:1592 (1980).
80. E. L. Church, "Interpretation of High-Resolution X-ray Scattering Measurements," *Proc. SPIE* **257**:254 (1980).
81. E. L. Church, "Fractal Surface Finish," *Appl. Opt.* **27**:1518–1526 (1988).
82. E. L. Church and P. Z. Takacs, "Instrumental Effects in Surface Finish Measurements," *Proc. SPIE* **1009**:46–55 (1988).
83. E. L. Church and P. Z. Takacs, "Prediction of Mirror Performance from Laboratory Measurements," *Proc. SPIE* **1160**:323–336 (1989).
84. E. L. Church and P. Z. Takacs, "The Optical Estimation of Surface Finish Parameters," *Proc. SPIE* **1530**:71–86 (1991).
85. E. L. Church and P. Z. Takacs, "Specification of the Surface Figure and Finish of Optical Elements in Terms of Systems Performance," *Proc. SPIE* **1791**:118–130 (1992).
86. J. E. Harvey and K. L. Lewotsky, "Scattering from Multilayer Coatings: a Linear Systems Model," *Proc. SPIE* **1530**:35–46 (1991).
87. Anita Kotha and James E. Harvey, "Enhanced EUV Performance of Wolter Type II Telescopes," *Proc. SPIE* **2011**:34–46 (1993).
88. Anita Kotha, "EUV Performance of Wolter Type II Telescopes for Space Astronomy Applications," M.S. thesis, Dept. of Physics, Univ. of Central Florida (1992).
89. William J. Gresslor, "Conical Foil X-ray Telescope Performance Predictions for Space Astronomy Applications," M.S. thesis, Dept. of Electrical and Computer Engineering, Univ. of Central Florida (1993).
90. J. E. Harvey, William P. Zmek, and C. Ftaclas, "Imaging Capabilities of Normal-incidence X-ray Telescopes," *Opt. Eng.* **29**:603–608 (1990).

91. K. L. Lewotsky, A. Kotha, and J. E. Harvey, "Performance Limitations of Imaging Microscopes for Soft X-ray Applications," *Proc. SPIE* **1741** (1992).
92. Kristin L. Lewotsky, "Performance Limitations of Imaging Microscopes for Soft X-ray Applications," M.S. thesis, Dept. of Electrical and Computer Engineering, Univ. of Central Florida (1992).
93. K. L. Lewotsky, A. Kotha, and J. E. Harvey, "Optical Fabrication Tolerances for Synchrotron Beamline Optics," presented at the (1992) *Annual Meeting of the Optical Society of America*, Albuquerque, NM (Sept 1992).